ORIGINAL ARTICLE

Wire arc additive manufacturing of thin and thick walls made of duplex stainless steel

Antoine Queguineur[1,2] · Reza Asadi[1] · Marta Ostolaza[3] · Emilie Hørdum Valente[4] · Venkata Karthik Nadimpalli[4] · Gaurav Mohanty[5] · Jean-Yves Hascoët[2] · Iñigo Flores Ituarte[1]

Abstract

Wire arc additive manufacturing (WAAM) direct energy deposition is used to process two different duplex stainless steels (DSS) wire chemistries. Macro- and micromechanical response variables relevant to industrialization are studied using a design of the experiment (DoE) approach. The tested operation window shows that the variation of layer height and over-thickness are highly correlated with travel speed and wire feed speed and positively correlated with heat input. The maximum achieved average instantaneous deposition rate is 3.54 kg/h. The use of wire G2205, which contains 5 wt% nickel content, results in a ferrite-to-austenite ratio that is equally balanced, while wire G2209, with 9 wt% nickel, provides a lower ferrite content. The spatial distribution of Fe% is influenced by part geometry and path planning, and higher heat inputs result in coarser microstructures. The manufacturing weaving strategy generates a heterogeneous microstructure characterized by fluctuations in Fe%. Thus, understanding the effect of complex thermal history, higher-dimensional design spaces, and uncertainty quantification is required to drive metal WAAM toward full industrialization.

Abbreviations

AM	Additive manufacturing
CAD	Computer-aided design
CMT	Cold metal transfer
CTWD	Contact tip-to-work distance
DoE	Design of experiment
DSS	Duplex stainless steel
Fe%	Ferrite content percentage
GMAW	Gas metal arc welding
HI	Heat input
HV_3	Hardness-Vickers-3kg load
IQR	Interquartile range
IT	Interpass temperature
OFAT	One-factor-at-a-time
SEM	Standard error of means
TS	Travel speed
WAAM	Wire arc additive manufacturing
WFS	Wire feed speed
XRD	X-ray diffraction

✉ Antoine Queguineur
antoine.queguineur@tuni.fi

1 Faculty of Engineering and Natural Sciences, Tampere University, Korkeakoulunkatu 6, 33014 Tampere, Finland

2 Ecole Centrale Nantes, GeM-UMR CNRS 6183, 1 rue de la Noé, 44321 Nantes, France

3 Dept. of Mechanical Engineering, University of the Basque Country (UPV/EHU), Torres Quevedo 1, 48013 Bilbao, Spain

4 Department of Civil and Mechanical Engineering, Technical University of Denmark, 2800 Kgs, Lyngby, Denmark

5 Materials Science and Environmental Engineering, Tampere University, Korkeakoulunkatu 6, 33014 Tampere, Finland

1 Introduction

Metal additive manufacturing (AM) has become a serious alternative for high-value industrial applications [1–3]. Directed energy deposition (DED) is a good candidate for large-sized AM applications and can be applied to many processes [4–9]. Powder or wire can be used as feedstock processed with an energy source based on laser, electric arc, electron, or induction, among other alternatives. DED provides the highest deposition rates in metal AM. In wire arc additive manufacturing (WAAM) processes, up to 5 kg/h

and a maximum of 10 kg/h rates can be attained for single wire and tandem systems [10–12]. In contrast, the electron beam additive manufacturing (EBAM) process can reach up to 19.8 kg/h rates [13].

Among all the metal AM direct alternatives, WAAM provides (i) high deposition rates, (ii) low investment and operation costs, and (iii) broad material selection. The working principle of WAAM is use of an electric arc as a power source and wire as feedstock. Available arc sources include tungsten inert gas, a plasma arc using a transferred arc, and gas metal arc welding (GMAW). Traditional transfer modes in GMAW are short circuit, globular, or spray transfer; however, synergic welding systems have been extensively used in both research and industry [14]. These synergic welding machines allow controlling both the electrical characteristics and the wire movements for dedicated materials, extending the range to lower energy. Consequently, it results in a wider range and better control of the heat input (HI), improved weld quality, and decreased spatter during deposition [15].

Among all the material alternatives in WAAM applications, duplex stainless steel (DSS) is attractive due to its good mechanical properties and high corrosion resistance, including against pitting corrosion. DSS has these characteristics thanks to the presence of ferrite and austenite in equal proportions (50/50). However, in welding applications, the ferrite content can vary due to the rapid thermal cycles involved [16, 17]. In the welding of dissimilar welds, for example, a DSS with a low alloy steel, the ferrite content is also affected by the dilution of the base materials into the melt pool [18]. To promote the formation of near-nominal ferrite-austenite contents with a tolerance of 30–70% of ferrite, wire manufacturers have adapted the chemical composition of their wire feedstock by increasing the nickel content to facilitate austenite formation at high temperatures.

Due to the large size and complexity of the parts, the thermal gradients involved in WAAM vary from welding to GMAW with longer cooling times. However, this statement depends on the welding application in GMAW and only applies to thick multipass welding. On the contrary, single-pass GMAW results in various grain structures and especially coarse microstructure at weld center with lower cooling rate and temperature gradient than close to the fusion line and heat-affected zone [19]. The utilization of DSS-optimized filler material in WAAM process, i.e., using a G 22 09 wire, becomes detrimental due to the 3 wt% of nickel added to the wire's chemical composition. It leads to a low ferrite content of approximately 30%. Indeed, Posch et al. reported 32% of ferrite on a thin-wall turbine blade [20] and Pechet et al. an average value of 30% on a thick wall for a hollow blade propeller application [21]. Both studies used a G 22 09 3NL wire and the measurements were performed with a Feritscope©. Alternative wire chemical compositions, closer to the original composition of DSS such as the GZ 22 05 3L, can be a good opportunity for WAAM products to increase the ferrite content in the matrix. Stuzer et al. measured 72% ferrite using this wire on a thin wall [22]. A vast range of ferrite content (25–65%) for similar material selection and similar geometrical configurations has been reported [23]. However, a high amount of ferrite is detrimental to the impact toughness, especially at low temperatures [24]. The thermal cycles in AM can lead to variation of the ferrite/austenite ratio and, consequently, better control of this ratio is interpreted as better control of the manufacturing process.

The grain growth during solidification is affected by the thermal cycles and process parameters in metallic AM as DED and powder bed fusion (PBF). As a result, the final microstructure and mechanical properties of the additively manufactured part may be anisotropic, which can affect its machinability. In particular, when considering parts produced by PBF, Perez et al. highlighted that the orientation of cutting tools toward columnar grains can affect cutting forces [25]. The surface roughness and waviness of as-built WAAM parts may also require post-treatment, highlighting the importance of considering grain morphology.

During a deposition in WAAM, a shielding gas protects the molten pool from the atmosphere and prevents oxidation. The gas mixture is usually composed of an inert gas such as argon (Ar) but can also include other elements like helium (He) as well as active gas like carbon dioxide (CO_2). Helium is known to increase the plasma energy and fluid flow in the molten pool, influencing the bead dimension and thermal behavior [26]. Adding carbon dioxide (CO_2) helps maintain arc stability and, as with He, improves the weld bead dimensions [27]. Finally, it has been reported that extra nitrogen in the gas mixture promotes austenite formation during welding [22]. Loss of nitrogen during the welding process can lead to pitting corrosion, thus adding nitrogen to the gas mixture and wire can reduce that risk [28]. Nitrogen loss is suggested to be more significant in WAAM than in welding applications [29]. A higher bead surface area in contact with the atmosphere in AM part than in a welding join may promote nitrogen to diffuse outside of the melt pool.

The primary purpose of a shielding gas in GMAW is to create a protective layer against the atmosphere, particularly oxygen (O_2). Lack of a proper shielding gas can lead to uncontrolled oxidation. With DSS alloys, pitting corrosion resistance is known to be reduced with higher oxygen content due to the formation of oxides and inclusions [30]. Many factors are involved in austenite formation; among them, wire composition, gas mixture [31], and thermal gradients [17] play a significant role. Furthermore, the relationship between power sources and the WAAM process parameters in synergic welding machines has not

been fully described in the literature, and they are therefore often treated as a "black box" [32, 33]. Eriksson et al. have investigated the effect of HI variation on the mechanical properties and microstructure for thin-wall super duplex stainless steel while fixing the other input parameters [34]. A comparison between the process parameters with other input parameters and the impact of a variation in wall geometry has yet to be proposed for screening purposes.

The wire feed speed (WFS) and travel speed (TS) have a direct effect on the window of operation, as they affect the achievable deposition rates and quality parameters in WAAM. Thus, they are strictly correlated with other process and response variables. The body of research shows that WFS and TS have a direct impact on the resulting macroscale geometry (i.e., resulting layer thickness, part height, and over-thickness as a function of process parameters) [29, 35]. They have also been reported to have a direct impact on hardness (HV_3) and Fe%, among others [23].

To this end, the novelty of this research is the study of the relationship between influencing process parameters within the WAAM process on DSS. We studied the WFS, TS, and interpass temperature (IT), as well as power source electrical measurements while exploring final quality response variables both at the macro- and microscale, which are relevant to industrialization. Moreover, current research is mostly limited to thin walls and simple shape welding paths [22, 36–40]. Thus, the impact of geometrical variation on thin and thick walls performance variables has not been fully explored. Geometrical dependencies and path planning strategies affect the thermal history of the part. This phenomenon has subsequent effects on the macro- and

microstructural properties. This research presents a comparative study of thick and thin walls that is closer to the industrial context, using two DSS wire chemistries.

To summarize, this research explores a range of influencing parameters based on identified research gaps. Its contribution is to (i) determine a window of parameters comparing DSS processed by WAAM-CMT. A systematic screening design of experiment (DoE) is proposed with a variation of two different wire chemistries, wire feed rates, travel speeds, and three interpass temperatures. Next is to (ii) evaluate the resulting macroscale geometrical results (i.e., resulting layer thickness, part height, and over-thickness as a function of process parameters) and finally (iii) evaluate the microscale results of mechanical properties including hardness (HV_3), resulting average ferrite content (Fe%), spatial distribution, nitrogen and oxygen in the matrix compared to the wire composition, and optical microstructural characterization. The nitrogen and oxygen analysis focuses on two thick wall samples with high and low HI to help interpret the results.

2 Materials and methods

2.1 WAAM equipment and sample manufacturing process

The power source used in this experiment was a FRONIUS TPS 4000. This GMAW synergic machine is also equipped with a cold metal transfer (CMT) unit, ensuring a low HI in a controlled short-circuit mode [15]. Figure 1b shows the welding torch integrated on a Yaskawa Motoman MH24, type

Fig. 1 Experiment setup: **a** printed walls, **b** Yaskawa robot, and **c** substrate deposition strategy
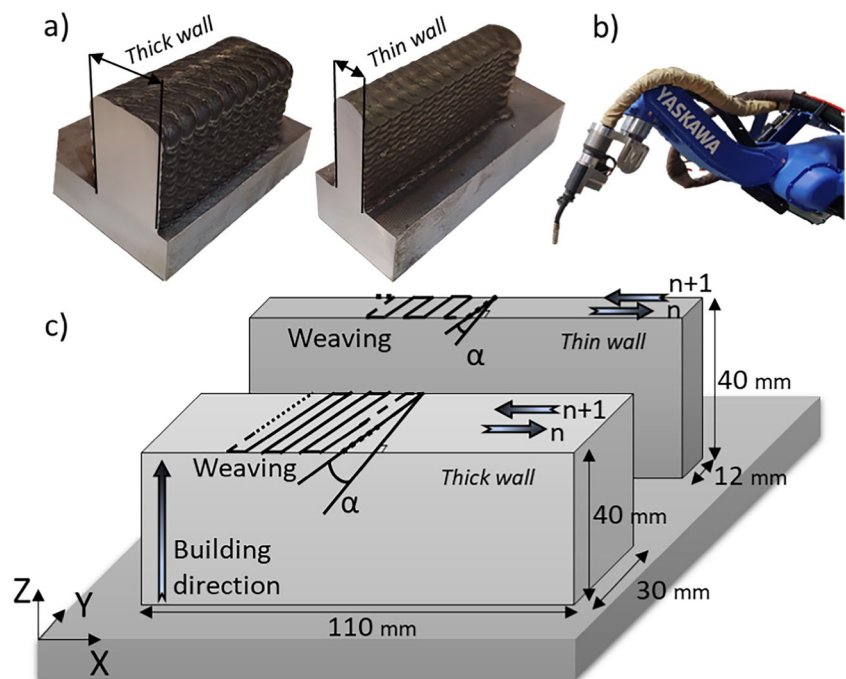
YR-MH24-A10, robot. Figure 1c illustrates the layer-by-layer metal deposition strategy using a specific welding path. It consists of weaving paths using a bi-directional deposition strategy including a square form at the edges and a weaving angle in the center of the walls with an angle of $\alpha = 30°$. This angle was obtained in previous trial and error experiments and is not considered a variable in the experiments. Industrial application may involve complex shapes leading to local rotations between the path planning and the part surfaces. Hence, α may vary throughout each deposition layer.

Irregularities at the start and end points of weld beads have been reported, as the arc-igniting portion is higher than the arc-extinguishing one [35]. Thus, in this study, each layer is alternatively deposited in opposite directions to maintain surface homogeneity.

The nominal dimensions of the walls were length 110 mm, height 40 mm, and thickness 12 mm and 30 mm for "thin" and "thick" walls respectively (Fig. 1a and c). The welding torch remained perpendicular to the welding direction with a contact tip-to-work distance (CTWD) of 15 mm in average. S355 (EN 10025-2) low-carbon steel plates of thickness 20 mm were used as the substrate (see Fig. 1a) and clamped to the worktable. Before deposition, the base plates were ground to remove any surface oxidation and cleaned with acetone to eliminate any impurities. The selected deposited material is an austenitic-ferritic grade steel commonly known as duplex. It has good weldability, stress-corrosion resistance, and relatively strong mechanical properties [22, 29, 41].

The microstructure of DSS consists of two phases (austenite and ferrite), usually in equal proportions. Depending on the final application and welding requirements, the wire's chemical composition is adapted, and a few variants proposed, by the wire manufacturer. In this study, a regular G22093NL (G2209) and a G22053NL (G2205) wire of diameter 1.2 mm were used. Table 1 shows the detailed chemical compositions of the filler materials as determined by the wire manufacturer. As the GMAW process requires using a shielding gas, a gas mix of ArHeCO2N-5/1,8/1,7 (EN ISO 14175: Z) was selected.

2.2 Formulation of energy input

GMAW uses an electric arc to fuse both the wire acting as the electrode and the workpiece metal. In the GMAW process, the CMT technology consists of a waveform control and mechanical inversion of the wire feed direction at optimized frequency. This particularity leads to a reduction of HI and spatters. CMT is a controlled short-circuit

deposition at low power range [15, 42] patented by Fronius©. Initially developed for welding thin plates, the process has found applications in cladding [43] and, by extension, WAAM for the same benefits of energy control.

Specific welding synergic lines are developed for each application and are considered "black boxes" due to the apparent complexity of the electrical signal. The most influential process parameters affecting melt pool formation are yet to be determined. The energy measurement provided by the welding machine during manufacturing is also important, as it affects the mechanical and microstructural properties of the deposited material. Too high energy may be detrimental to the mechanical properties of the manufactured components and lead to loss of corrosion resistance of DSS [44, 45]. Equation (1) describes the energy according to the standard EN ISO 1011-1.

$$HI = \eta \times \frac{V \times I}{v} \times 10^{-3} \quad (kJ/mm) \tag{1}$$

where "η" refers to the process/thermal efficiency and is considered to be $\eta = 0.8$ for GMAW, "V" is the welding voltage (V), "I" is the welding current (A), and "v" is the welding speed (mm/s). The compound value HI refers to the heat input measured in kJ/mm.

Measurement of HI is the de facto standard in the WAAM process, as it is based on welding technology. Most of the literature available uses this compound variable for parameter optimization and characterization [29, 33, 35, 44, 45]. HI evaluation is critical and can lead to significant errors [33]. Hence, it is recommended to follow the approach described in ISO/TR 18491. The measurement device requires a high sampling frequency to measure the synergic changes. The recommendation of instantaneous measurements is aimed at more accurate measurements of the HI, due to the complexity of the signal in the CMT process.

The CMT process allows a small variation of the WFS and, consequently, it can affect the deposition rate at the margins. The deposition rate can be estimated as an instantaneous or global deposition rate. Waiting time between layers is considered in the global deposition rate, which is directly linked to external factors such as the size of the part to be printed, the substrate, and the interpass temperature. The instantaneous deposition rate only considers the time during manufacturing and is therefore independent of the sample size and configuration of the part.

Table 1 Filler metal chemical compositions—3.1 certificates (EN 10204-1)

	C	Si	Mn	Ni	Cr	Mo	Cu	P	S	N
G 22093NL, wt%	0.012	0.45	1.61	8.74	22.84	3.07	0.06	0.016	0.003	0.134
G22053NL, wt%	0.020	0.50	0.80	5.10	22.40	3.10	-	0.028	0.001	0.170

2.3 Design of experiment (DoE)

Design of experiments (DoE) is an effective method to screen, model, and optimize the response variables (i.e., outputs) by systematically modifying process parameters (i.e., inputs) [46–48]. In this research, a one-factor-at-a-time (OFAT) method was implemented to screen parameter correlations in the WAAM process for thin and thick walls made with two different DSS wires. OFAT experiments vary only one factor or variable at a time while keeping others fixed to consider the impact of each input. The primary goal of this analysis was to screen the set of parameters while considering the sensitivity and behavior of the process outputs. Thus, the OFAT method was sufficient for our screening purposes.

2.3.1 Process parameters

Table 2 shows the process parameters and levels of the OFAT experiment. We included five process parameters including the IT with three numeric levels, the WFS, the TS, the block thickness with two numeric levels, and the wire chemical composition with two categorical levels.

Three IT levels were explored: 100 °C, 150 °C, and 250 °C. DSS can be sensitive to intermetallic precipitation during manufacturing [3, 49]. Excessive ITs can lead to longer times above the critical temperatures of 300–900 °C, affecting the final microstructure such as precipitation of intermetallic phases and the properties of the material. Sigma (σ) and χ phases can precipitate at a higher range of 600–900 °C [50, 51] with chromium nitrides (Cr_2N) and chromium carbides [52], while at lower temperatures of 300–600 °C, π phase, Z phase [53], and embrittlement of the G phase can occur under exposure exceeding 1000 h [54]. Before manufacturing, the substrates were preheated at 100 °C using a resistance heating system. The thermal data required to control the IT set by the DoE were recorded every 1 ms using a PicoLog TC08 data logger with K-type thermometers (−270 °C, +1370 °C).

Figure 1a and c show the selected block thicknesses including thick (30 mm) and thin (12 mm) walls. The welding path utilizes the dimensions corresponding to the "nominal CAD"

wall thicknesses. The thermal behavior during manufacturing can be affected by the wall thickness, either reducing or increasing the heat evacuation owing to conduction within the part. Previous studies mostly investigated a single-pass multilayer configuration [22, 36–39]. However, few authors have tested weaving [20] and multi-bead walls [29]. In this work, the thinner and thicker walls were produced using a weaving technique and a square form welding path to achieve thicker dimensions. Each configuration was a single-bead multilayer configuration, and the length was fixed at 110 mm. The location of the start and end points was not optimized and therefore is not considered in this study.

As mentioned above, two filler materials were selected with relatively similar compositions except for the nickel content (see Table 1) acting as an austenite stabilizer. Consequently, in similar welding conditions, a higher amount of ferrite in the G2205 samples compared with the G2209 samples was expected.

The CMT process allows fluctuation of the WFS, thus impacting the weld bead dimensions. The electrical parameters are linked to a specific WFS. Modification of a set of parameters is, however, possible, such as arc length correction and dynamic correction [15]. Table 3 shows the assumed HI corresponding to a selection of theoretical electrical parameters (current I and voltage V) at a certain set of WFS and fixed TS. The high HI set uses a TS of 720 mm/min associated with a WFS of 7.4 m/min (211(I)/16.4(V)). Then, a low HI is proposed with a TS of 1320 mm/min and a WFS of 5.4 m/min (172(I)/14.7(V)).

2.3.2 Response variables

During this experimental work, the focus is on response variables that are interesting from an industrialization viewpoint. To do so, the list of response variables can be grouped as (i) macro-results (i.e., resulting layer thickness, over-thickness, time per layer, achievable instantaneous, and global deposition rate) and (ii) micromechanical properties (i.e., hardness Hv3, ferrite content Fe%, and microstructural characterization).

Table 4 details the relevancy of other response variables such as in-process electrical parameters and chemical changes in terms of nitrogen and oxygen.

Macroscopic geometrical measurements were performed on a SIP-CMM5 3D coordinate measuring machine with a

Table 2 Theoretical input variables

Process parameters	Level		
	1	2	3
A: IT (°C)	100	150	250
B: WFS (m/min)	5.4	7.4	-
C: TS (mm/min)	720	1320	-
D: Block thickness (mm)	30	12	-
E: Wire chemical composition	G22 09	G22 05	-

Table 3 Nominal values of electrical parameters

Heat input (kJ/mm)	WFS (m/min)	Current(I)/ voltage (V)	TS (mm/min)
High HI, 0.23	7.4	211/16.4	720
Low HI, 0.09	5.4	172/14.7	1320

Table 4 Relevance of response variables toward industrialization

| Response variables		Relevance toward industrialization
Macromechanical	Layer thickness	Improved understanding of the manufacturing process affecting the stability of the stick-out, tip-to-work distance (CTWD), deposition rates, and productivity parameters including manufacturing cost
	Over-thickness	Improved understanding of the manufacturing process affecting control of material waste and reduction of post-processing, material, and manufacturing costs
	Time per layer	Improved understanding of the manufacturing process affecting life cycle costs (LCC), productivity, and achievable deposition rates, manufacturing costs
	Instantaneous and global deposition rate	Improved understanding of process parameters affecting WAAM productivity parameters toward industrialization and manufacturing costs
Micromechanical	Hardness	Improved understanding of process parameters affecting the hardness mechanical properties
	Ferrite content	Improved understanding of process parameters affecting mechanical properties and corrosion resistance characteristics
	Microstructural characterization	Improved understanding of process parameters affecting the achievable microstructural characteristics
Others	In-process electrical parameters	For quality control purposes. Promotes control of manufacturing constraints
	Chemical changes	Improved understanding of process parameters affecting the variation of chemistry for pitting corrosion resistance

resolution of 0.1 µm and repeatability $R = 0.2$ µm. As the explanation for the resolution and repeatability, resolution denotes the smallest measurable modification in a variable, while repeatability indicates the level of coherence in successive measurements of that same variable under the same conditions. Geometrical measurements focus on the height and width of each wall. Figure 2a shows how high internal stress levels can lead to plastic deformation of the substrate during manufacturing. Hence, considering the height measurements, the reference plane is located in the least deformed area, which is the central area of the substrate, close to the middle of the wall. Figure 2a shows the location of the height measurements and an average value is proposed based on nine measurements along the top surface. The layer height is estimated based on the height of the wall divided by the number of layers. The wall thickness is calculated based on the external faces of the wall. One of the faces is

set as a reference plan. The thickness is obtained based on the external measurements performed on the opposite side. The over-thickness in this study is a comparison between the measured and nominal (by design) thickness of the walls.

Hardness measurements were conducted using a Duramin-A300 hardness testing system and Vickers method with a 3-kg load for 15 s according to the standard EN ISO 6507. Figure 2b shows the measurements performed every 1 mm on a vertical line central to the cross-section. The cross-sectional samples were prepared by metallographic grinding and polishing down to a 3-µm diamond suspension.

Before micrographic examination, the samples were ground and then polished down to 1-µm diamond particles. The selected etchant was Beraha's II (H20-HCl-K2S2O5). Varbai et al. used Beraha's II as a color etchant for ferrite/austenite ratio quantification [55]. The etchant colors the ferrite phase while keeping the austenite phase bright and

Fig. 2 Geometrical measurements: **a** substrate deformation and height measurement, **b** HV3 measurements, view of vertical testing line
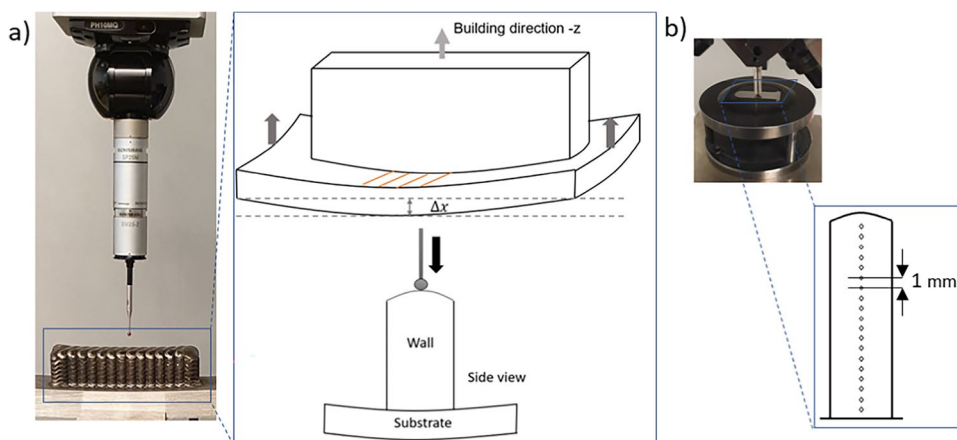
unetched. Microstructural observations were conducted using a Leica DMi8 optical microscope from the bottom to the top of the samples. Three pictures at the bottom, middle, and top parts of the sample were taken for each sample. Finally, the ferrite/austenite ratios were measured using the image processing ImageJ software.

Previous studies have proposed a comparison between different measurement methods to determine the ferrite content [56, 57]. The three main methods used for ferrite determination are X-ray diffraction (XRD), image analysis, and Feritscope©. XRD is a quantitative method for determining crystalline phases and is not appropriate for global ferrite content evaluation in WAAM DSS, since XRD provides highly localized measurements. Therefore, for WAAM coarse structures and due to the heterogeneities of the process itself, more variation in the results is observed with XRD than with the other testing methods. The image analysis method has proved to be the most accurate method for ferrite content evaluation and is associated with Beraha's II etching, which is considered to be the reference method. However, variations in the etching procedure and between operators can lead to a lack of repeatability of the ferrite measurements. Moreover, to provide a complete screening of a sample, a high number of areas should be evaluated to minimize the discretization error. This method is therefore time consuming and resource intensive, which is not admissible for a large DoE-based methodology. Regarding the Feritscope©, uncertainty of measurements compared to image analysis can be caused by the (i) conversion curve between ferrite number (FN) and Fe% proposed by the manufacturer (FISCHER) leading to an uncertainty of $\pm 7.5\%$ (relative) for ferrite, or even $\pm 10\%$ over 70FN, or (ii) impact of the magnetic field during measurement of up to 1–2 mm in the sample volume [56]. However, the Feritscope© is an interesting approach for estimating ferrite content and provides a good balance between accuracy and resource consumption.

In this study, a complete longitudinal and transverse 2-dimensional screening of the walls was done using the Feritscope© method with a probe mounted on an Ender-3Pro from Creality-3D. Previous research has mentioned manual and localized measurements of the sample's surfaces [20, 56, 57]. In this study, a complete automatized screening of the sample surfaces was performed with a measurement every 1 mm in the Z and Y directions on the cross-section of the walls. The edges corresponding to a distance of less than 2 mm from the surface of the wall were not considered in this study due to interaction of the magnetic field with the edges. To provide a similar surface roughness, the samples were ground. The Feritscope© is a FMP30-FISCHER machine using a FGAB1.3-Fe probe. An approach speed "v" of less than 4 mm/s was set with a lift-off distance of 20 mm between two points.

Image analysis was carried out to provide a complete evaluation of the ferrite content and was done on just a few samples from the DoE. The characterization consists of color segmentation based on the contrast—darker gray (DGP) and lighter gray (LGP)—obtained between the austenite and ferrite in the etched samples [55]. The boundary value (DGP + 0.5 * ΔG) is considered, with ΔG being the difference between the two gray level peaks. Finally, a comparison between the image analysis method and Feritscope© measurements is proposed to demonstrate the suitability of the Feritscope© for this purpose.

During the experiments, the power source signal corresponding to the electrical parameters, including intensity (I) and voltage (V), was recorded. These measurements were based on the internal device signal system provided by the welding power source. The sampling rate of the device was one measurement per 7.16 μs. Then, an average value was calculated every 10 ms. A resulting HI per layer based on measured electrical parameters is presented in this study. Parameters such as WFS can vary during the process of deposition. These were recorded and presented as an average value per layer.

The nitrogen and oxygen content evaluation in the deposited walls was measured by instrumental gas analysis (IGA) on a LECO TC500 following the requirements of the E1019-11 ASTM standard. Nitrogen promotes the austenitic phase in the matrix and, therefore, influences the final ferrite-to-austenite ratio. The determination of the resulting nitrogen content after deposition provides a better understanding of the phenomena involved in this study. The evaluation of nitrogen and oxygen focused on the deposited walls using the highest and lowest HI for both materials. The walls were machined avoiding the first diluted layers and the chips were then cleaned with ethanol in an ultrasonic bath, followed by cleaning in acetone and drying. A sample typically weighs 0.2 ± 0.02 g and the two wires were tested as a reference for the study.

2.4 ANOVA—analysis of variance and statistical methods

The study used data analysis methods to establish the statistical relationship between process and response variables as presented in Del Sol et al. and Asadi et al. [58, 59]. The analysis of variance (ANOVA) was applied to assess how independent variables correlated with dependent variables at a 95% confidence interval. ANOVA introduced different terms including R^2, which measures how variations in one variable can be correlated with differences in a second variable. The study used a robust and reliable version of R^2 known as R^2_{adj}, with significant correlation attributed to R^2 and R^2_{adj} values greater than 0.85. The P-value was also employed to confirm the significance of welding-independent parameters based on linear relationships of input-output sets, with P-values

below 5% indicating significant parameters. To support the analysis, factor plots and Pareto charts were created. Outlier detection was performed to assess whether the acquired experimental data was suitable for further analysis. Quantile range and robust fit methods were used to identify potential outliers that deviated from the normal pattern of the data. Robust fit outliers provided various estimates of the center and spread of data, including Huber, Cauchy, and quartile. The Cauchy option assumed a Cauchy distribution with a high breakdown point for the calculation of center and spread and was used to determine outlier thresholds.

3 Results and discussion

3.1 WAAM-CMT measured electrical parameters

CMT synergic lines are expressed as the relationship between the welding power source (i.e., the electrical parameters including current and voltage) and the resulting power as a function of process parameters, namely WFS. It should be mentioned that during manufacturing, external parameters such as stick-out and the position of the ground cable can affect these parameters. Figure 3 provides the experimental data points colored based on their heat input values, fitted regression line to the data points, and the 95 percent confidence area shaded in the figure. A 95% confidence interval is a range of values containing the true response parameter with a 95% probability. It also shows that the wire chemical composition does not have a significant impact on the relationship between power (P) and WFS.

Results show an approximately linear correlation exists between P and WFS (see Fig. 3). A wider variation of P and measured WFS can be noticed for a dedicated fixed WFS of 7.4 m/min. It shows a stronger instability than with a lower WFS of 5.4 m/min.
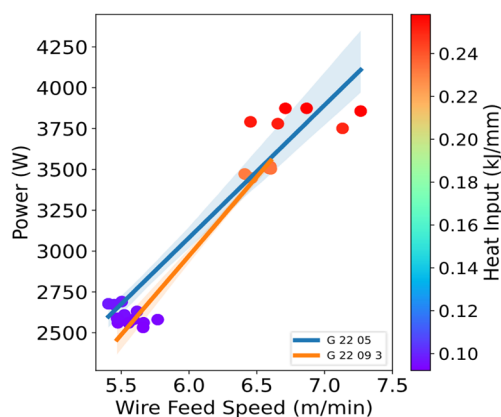
Fig. 3 Comparison between the measured WFS and power as a combination of I(A) and V(V)

3.2 Process parameter sensitivity analysis

Before starting the screening and analysis of the acquired data, checking the dataset to determine potential outliers and measurement errors is crucial. First, in this section, an evaluation of the experimental data is conducted to identify potential outliers. Second, the measurement errors are evaluated and, following that, the correlation is given between the input-output sets and ANOVA details.

3.2.1 Evaluation of outliers and measurement error

Two criteria, quantile range and robust fit, were used to detect outliers. The quantile range method used a tail quantile of 0.1 and a quantile of 3 by default. The robust fit method used the Cauchy option with $K=4$. The analysis showed that no outliers were identified by either criterion, indicating that the captured data and observations were consistent with the dataset's average or norm.

The OFAT design specified the analysis's purpose as screening, correlation finding, and overall input-output relationship determination. Because hardness measurements were destructive and could not be repeated at the same position, and the HV3 measurement device had a maximum deviation of 3% in the current hardness range, the experimental results were considered reliable.

The error measurements for ferrite content percentage were calculated using two different methods. The first method involved measuring Fe% across the entire cross-section of the workpiece, which showed a visible range of changes (Fig. 6). This method not only repeated the measurement tests but also evaluated Fe% variations within the proposed surface, with an average error of 9.5% based on 24 measurement points. The second method involved repeating measurements at a specific point using a 3-axis device, resulting in negligible uncertainty and measurement error (less than 0.001 after 40 measurements).

3.2.2 ANOVA tests, correlation map between process and response variables

This section is divided into two parts: (i) screening of HI as a reference variable for process parameter optimization and (ii) detailed screening of defined outputs based on the process inputs presented in Tables 2 and 3, with the aim of identifying the most sensitive parameters to output variation.

Using HI as a thermodynamic parameter from Section 2.2, this study aims to optimize process parameters by evaluating the sensitivity and variability of process inputs. Despite not providing a complete description of the process phenomena, HI is used as a reference variable. The

Table 5 Amounts of R^2, R^2_{adj}, and RMSE for HI in terms of two proposed wire chemical compositions for all proposed inputs

Thermodynamic parameters	HI	
	G22 05	G22 09
R^2	0.999915	0.999977
R^2_{adj}	0.999866	0.999963
RMSE	0.000964	0.000438

Table 6 Amounts of R^2, R^2_{adj}, and P-values for HI in terms of two proposed wire chemical compositions for each proposed output

Thermodynamic parameter		HI	
		G22 05	G22 09
Fe%	R^2	0.682184	0.465827
	R^2_{adj}	0.650402	0.41241
	RMSE	1.184446	0.447867
	P-value	0.00093	0.01446
HV_3	R^2	0.691018	0.711873
	R^2_{adj}	0.66012	0.68306
	RMSE	2.161447	1.866136
	P-value	0.00081	0.00056
Over-thickness	R^2	0.985637	0.991726
	R^2_{adj}	0.984201	0.990899
	RMSE	0.142357	0.088791
	P-value	0.000001	<0.000001
Layer height	R^2	0.850911	0.965972
	R^2_{adj}	0.836002	0.962569
	RMSE	0.033708	0.054326
	P-value	0.00002	<0.000001

screening results in Table 5 indicate that HI is significantly sensitive to input variations for two proposed wire chemical compositions, with R^2 considerably near 1. Overall, the studied criteria (including R^2, R^2_{adj}, and RMSE) suggest a slightly better correlation between input parameters and HI for G22 09.
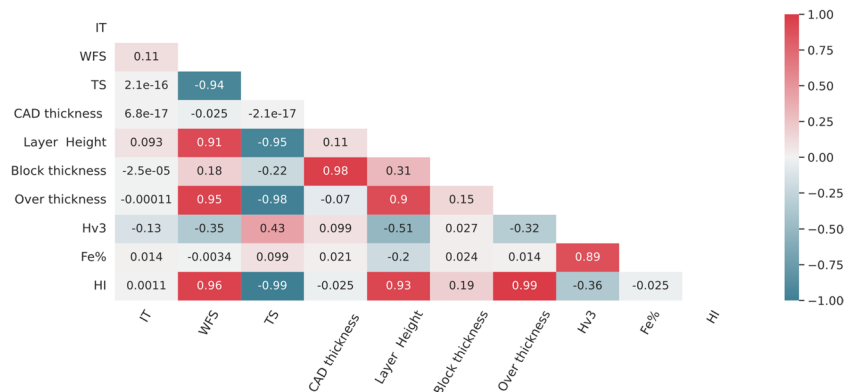
Table 6 shows the sensitivity of outputs to the variation of HI. It can be concluded that HI is not capable of fully capturing the variation of HV_3 as an output for the selected parameters. Selecting a wider range of parameters could have influenced the hardness results more significantly, and thus, further tests could be conducted toward this objective. The ANOVA tests show that over-thickness is linearly correlated to HI. For example, HI alone can explain 98.56% of the over-thickness variation for material G2205 and 99.17% for G2209. Similarly, HI can explain 85.09% and 96.59% of layer height variability for G2205 and G2209, respectively.

It can be inferred that all the outputs, except for HV_3, could be correlated linearly with the thermodynamic parameter. Thus, HI can be used as a thermodynamic compound variable to study the variation in WAAM processes.

The correlation between the different pairs of input and/or output sets can provide good insight into the experiments. Figure 4 shows the correlation map of the mentioned pairs and positively or negatively correlated parameters are highlighted from white (no correlation) to red (positively correlated) to blue (negatively correlated). It can be inferred that HI is positively correlated with the variation of macro-performance variables (i.e., layer thickness and over-thickness).

Regarding mechanical performance variables, HI fails to fully describe their variation. Hardness is important to determine a material response to a plastic deformation. However, this technique does not aim to be used as a quantitative indicator for the material mechanical behavior and cannot fully describe the mechanical performances. Other mechanical tests as tensile and impact tests may be more representative for describing the HI variation and could be implemented in further research.

However, interestingly, Fe% and HV_3 are positively correlated. An increase in Fe% leads to higher HV_3 on the manufacturing samples and an increase in energy applied (i.e., HI) leads to a decrease of HV_3 as it appears to be negatively correlated. From the process parameters'

Fig. 4 Correlation map between all pairs for the combination of inputs and outputs. Red denotes positive and blue denotes negative correlation

perspective, TS and WFS appear to be the most significant variables, thus driving the variation of macro- and micro-performance variables. TS and WFS show an opposing effect on the performance variables. WFS is linked to HI, as this phenomenon shows a correlation with electrical parameters in CMT process. A higher WFS value is positively linked to a higher HI value. Conversely, TS is one of the variables in the HI equation, and an increase in TS value leads to a decrease in HI value.

Finally, an ANOVA and regression analysis was performed on each output with respect to the assumed inputs based on wire material (G2205 and G2209). Table 7 presents the results of the criteria used to evaluate the sensitivity of dependent variables to proposed input parameters. Whereas there are some differences between the two proposed material compositions, most of the outputs except for HV_3 are sensitive to at least one input parameter, with a correlation rate criterion (R^2) greater than 85% for these parameters.

3.3 Macro-results: layer thickness, over-thickness, and deposition rates

Figure 5 shows the factor plot for the macroscale results (i.e., over-thickness and layer height) as a function of IT, WFS, TS, and CAD thickness for both filler materials. The linear fits on the factor plot show what the ANOVA table unveiled. Both macro-results are most sensitive to the variation of WFS and TS. Wall thicknesses described as CAD thickness and IT have lower statistical significance. In other words, the variation of these two parameters has less effect on the macro-results.

It is worth mentioning that both filler materials (G2205 and G2209) show very similar trends. Both materials are highly sensitive to WFS and TS variation. Increasing WFS has a direct effect on achievable layer height and over-thickness, whereas the increase of TS has the reverse effect. Increasing WFS leads to an increase in the amount of material deposited. Conversely, increasing TS leads to a decrease in material deposition per unit length.

Table 7 Analysis of the sensitivity of dependent outputs to the proposed independent inputs in terms of two different wire chemical decompositions

Output	Wire material					
	G22 05			G22 09		
	R^2	R^2_{adj}	RMSE	R^2	R^2_{adj}	RMSE
Fe%	0.90135	0.844978	0.788727	0.729768	0.57535	0.380739
HV_3	0.799367	0.684719	2.081757	0.809491	0.700628	1.813679
Over-thickness	0.993868	0.990363	0.111181	0.992756	0.988617	0.099300
Layer height	0.922728	0.878572	0.117053	0.987438	0.98026	0.039451
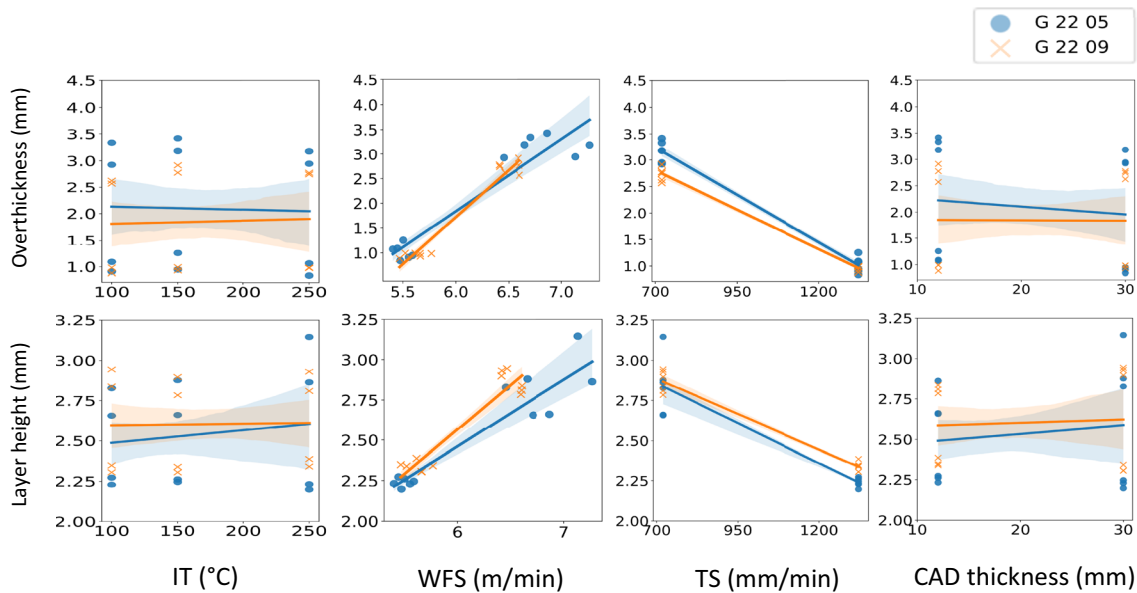
Fig. 5 Factor plot for layer height and over-thickness as a function of IT, WFS, TS, and CAD thickness

The deposition rate varies based on the selected outputs. The average values of the instantaneous deposition rates are 3.54 kg/h with a WFS of 7.4 m/min and 2.94 kg/h with a WFS of 5.4 m/min. However, the average value of the global deposition rate remains similar between the two chosen WFSs (0.36 kg/h). Conversely, while the instantaneous deposition rates remain stable at 3.25 kg/h for thin walls and 3.23 kg/h for thick walls, the global deposition rate is higher for the thick wall than for the thin wall (0.5 kg/h and 0.2 kg/h, respectively). A thicker wall facilitates thermal conduction and shortens the waiting time between layers. This behavior is strongly linked to the size of the produced part.

3.4 Ferrite and austenite content and distribution

Figure 6 shows the factor plots for the average Fe% variation between samples based on the Feritscope© measurements as a function of HI using complete cross-section screening. The overall trend shows that for both wire chemistries, increasing the HI leads to a slight reduction of Fe% across the experimental window. The average Fe% for G2205 is 49.20% ± 1.92, whereas G2209 provides a reduced Fe% average of 29.69% ± 0.56, which shows a reduction of 19.5%. Increasing the HI applied to the WAAM of DSS decreases the Fe% by approximately 10.69% for G2205 and 5.88% for G2209.

Figure 7 shows the factor plot of the single effect of process parameters over the Fe%, and both materials show the same trend. WFS and TS are the most statistically significant process parameters with a direct effect on the variation of Fe%. The filler materials used in this study correspond to the welding industry requirements and only a few companies have recently been adapting the wire chemical composition to the AM constraints. The main impact of an increase in ferrite content is improved strength, but, on the other hand, less austenite leads to lower corrosion resistance and ductility. All in all, the material chemistry is the major contributor to the resulting Fe% with the considered parameters.

The previous analysis covers the variation in average Fe% values without considering potential variations across the sample. For this purpose, we used a Feritscope© mounted on a 3-axis machine. Figure 8 shows the Feritscope© setup to map Fe% variation across the samples, as well as example results of Fe% variation on longitudinal and transverse faces of the sample with colormaps representing the obtained Fe% distributions.

Figure 9 shows the front view of Fe% distribution for both filler materials for thick and thin walls with high HI (i.e., 0.23 kJ/mm—nominal value) and low HI (i.e., 0.09 kJ/mm—nominal value) at all tested ITs. The samples show a higher Fe% of about 5% on the upper parts of the cross-sections. These areas correspond to the last layer of the walls and therefore to a weld bead that was not subject to further reheating, which eventually tends to increase austenite

Fig. 6 Linear regression plot/fit plot and measurement intervals for each parameter between HI and Fe%
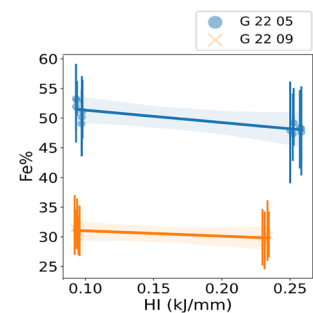
precipitation. During solidification of the melt pool, epitaxial growth of the ferrite grains is followed by a ferrite-to-austenite transformation in a solid state in the temperature range 1300–800 °C. This austenitic precipitation, occurring at the grain boundary of ferrite and then within the ferrite grain, is enhanced by a longer time within the critical temperature range of 1300–800 °C. Reheating cycles consecutive to the layer-by-layer deposition process leads to a slight decrease in Fe% in the central and lower areas of the cross-sections as shown in Fig. 9, with a predominance of green and yellow in both materials. This phenomenon is enabled if the temperature exceeds 800 °C, characterized by austenite precipitation toward a more stable state. Overall, the Fe% distribution is heterogeneous, with a dependency on part geometry within the cross-section of the part. It has been shown in the statistical analysis that the sensitivity of the wall thickness to variation of the output parameters such as average Fe% is not significant. However, the details provided in Fig. 9 reveal higher local heterogeneity with a dependency on part geometry within the cross-section of the part.

The lower parts of the walls correspond to the interface between the substrate (i.e., low-carbon steel) and the deposited DSS. This interface was not evaluated in this study. However, the substrate corresponds to the red color showing the predominance of ferrite. The subsequent low Fe% green layer is interpreted as diluted layers with a strong thermal influence of the substrate. For the thick walls and high HI, this area is 5 ± 1 mm in height and for the thick walls at low HI the area is estimated at 3 ± 1 mm. The penetration depth of the welding pool at high HI is higher than at low HI, affecting the partial dilution of the previous layer. This finding needs to be evaluated in further research and especially by studying the thermal impact of the substrate on the first layers. As shown in Fig. 9, higher Fe% can occur on the side of the walls and may result from a higher cooling rate due to environmental factors like an air extraction system. However, another variation of ferrite appears in the parts and particularly the thicker walls. The repetitive patterns tend to suggest that the welding path influences this behavior. This proposition is confirmed by subsequent longitudinal 2D colormaps of two samples of both the investigated materials.
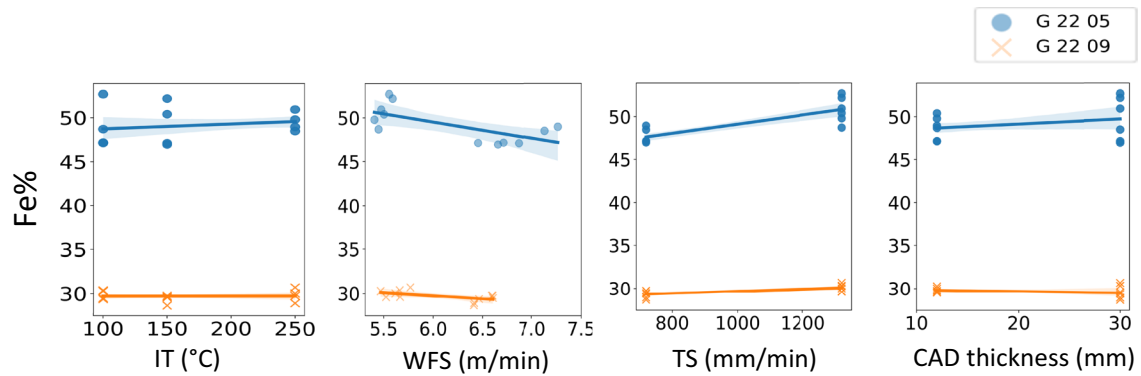
Fig. 7 Factor plot for Fe% as a function of IT, WFS, TS, and CAD thickness

Fig. 8 Example showing 2D colormap results of Fe% across transverse and longitudinal faces of the samples
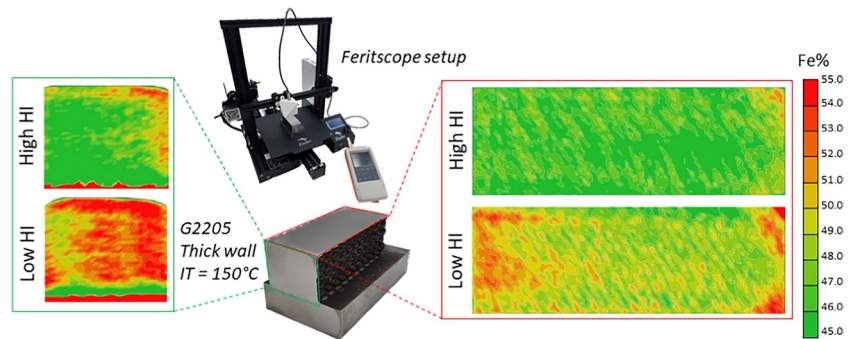

Figure 10 demonstrates how the implemented path plan and manufacturing weaving strategy affect the homogeneous distribution of Fe% across the sample. The observed trend is that Fe% distribution is more heterogeneous in samples produced with low HI (see Fig. 10b). Additionally, the extreme ends of the samples show a higher Fe%. Two main hypotheses are proposed to explain this. First, the grain orientation within the weld bead during solidification and the grain size in the grain growth zone of the heat-affected zone (HAZ) influence the magnetic field during Feritscope© measurements. As a Feritscope© applies a magnetic field to a specimen, an induced response of the material to the magnetic field is measured. The grain structure influences the magnetic response of the material. Hence, a modification of the grain size and orientation affects the induced magnetic field and consequently the ferrite content measurement. Another justification of the heterogeneous Fe% distribution is that local thermal gradients during manufacturing can affect the ferrite/austenite ratio. As the weld bead solidifies, a heat-affected zone (HAZ) is produced which reaches the temperature range of 1300–800 °C. This results in the precipitation of austenite, causing a deviation in the ferrite measures obtained with the Feritscope©.

It was noticed that the G2209 walls (see Fig. 9c and d) have a more homogeneous ferrite content than the G2205
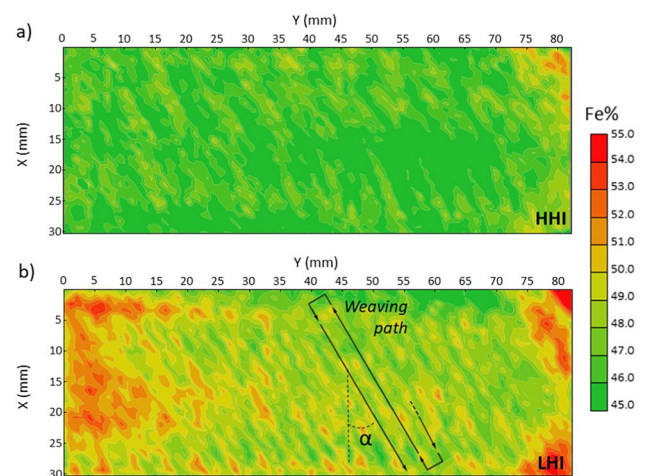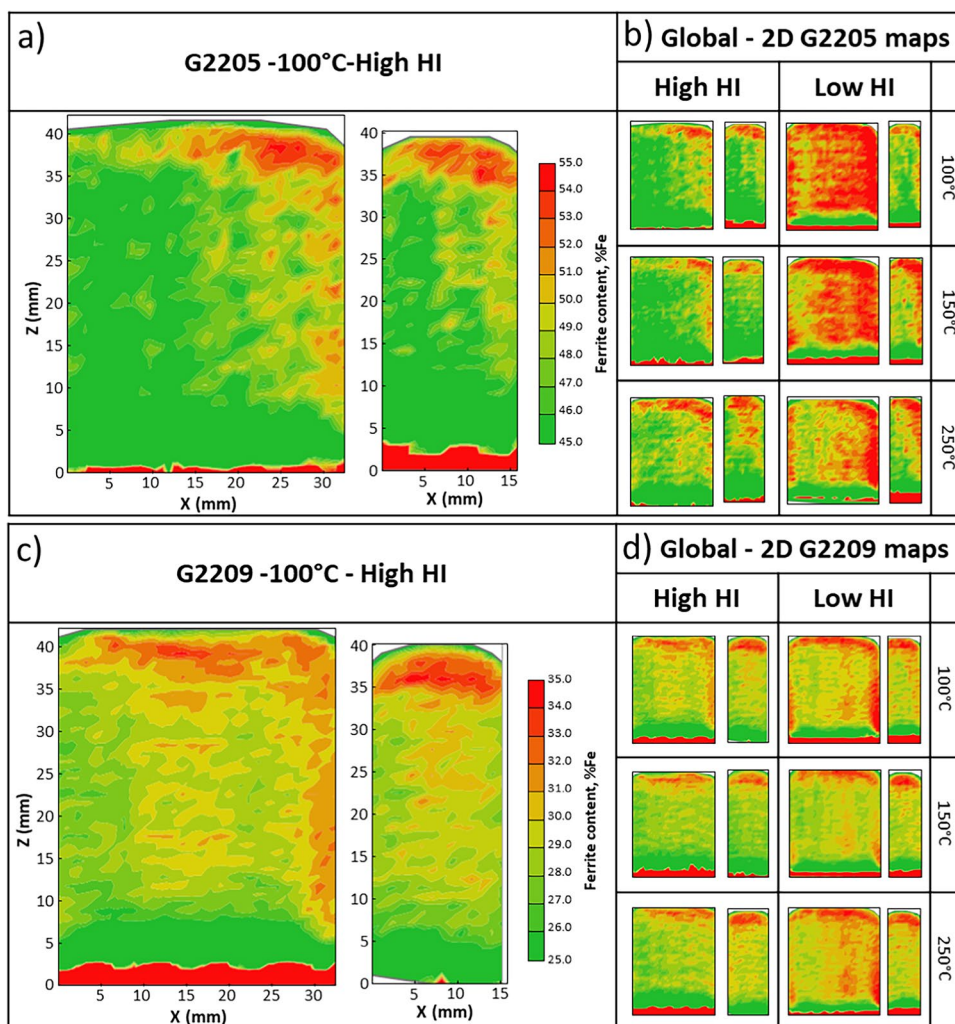
walls (see Fig. 9a and b). A proposed explanation is that G2205 is closer to a window of parameters the modification of which will affect the final microstructure. The plots in Fig. 11 support this statement with more variation in the results. On the other hand, G2209 showing less heterogeneity suggests that the material is in a more stabilized/equilibrium condition. This G2209 material is being developed and used for a welding application that does not require further heat treatment with an adjusted chemical composition to promote a 50/50 ferrite-to-austenite ratio in welding conditions. The strong thermal gradients involved in welding differ from the WAAM process, leading to the present results. Further research on G2209 could consider the use of external systems to enhance faster cooling, such as air, water, or cryogenic cooling, to promote higher Fe% within the material.

3.5 Hardness characterization

Figure 11 shows the resulting average HV_3 variation per sample as a function of HI. The overall trend shows that for both wire chemistries, increasing the HI leads to a slight reduction of hardness across the tested experimental window. The average hardness for G2205 is 282.5 HV ± 3.55, whereas G2209 provides a reduced hardness average

Fig. 9 Cross-section ferrite map. **a** G2205, interpass temperature 100°C, high HI; **b** G2205 compilation of 2D maps; **c** G2209, interpass temperature 100°C, high HI; **d** G2209 compilation of 2D map


Fig. 11 Linear regression plot/fit plot and measurement intervals for each parameter between HI and HV_3

Fig. 10 Fe% distribution across the longitudinal section—**a** G2205, high HI, and IT 150 °C; **b** G2205, low HI, and IT 150 °C
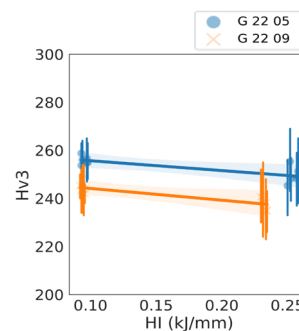
of 241.6 HV $\pm$ 3.31. The approximate reduced hardness for G2205 and G2209 with the increase in HI is 2.61% and 2.26%, respectively.

Figure 12 shows the factor plot of the single effect of process parameters over HV_3. Both materials show the same trends. WFS and TS are the most statistically significant process parameters with a direct effect on the variation of HV_3. As WFS is correlated with the electrical parameters, a higher
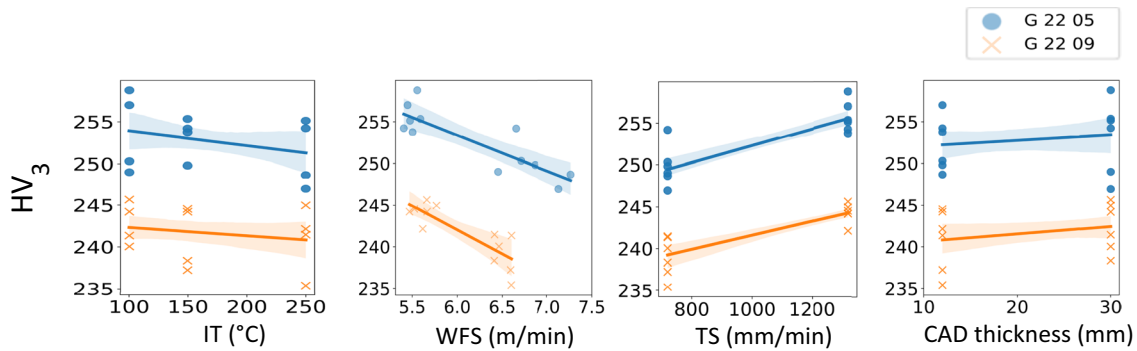
Fig. 12 Factor plot for HV_3 as a function of IT, WFS, TS, and CAD thickness

Table 8 Average HV_3 values and associated standard deviation

Sample process parameters		Thin walls		Thick walls	
		HV_3	Std dev.	HV_3	Std dev.
G2209	High HI—100 °C	241.35	5.17	240.05	5.78
	High HI—150 °C	237.25	5.80	238.34	5.38
	High HI—250 °C	235.40	4.65	241.46	5.77
	Low HI—100 °C	244.21	4.58	245.66	4.33
	Low HI—150 °C	244.54	5.30	244.21	4.54
	Low HI—250 °C	242.15	6.21	244.97	4.28
G2205	High HI—100 °C	250.31	4.33	249.00	4.05
	High HI—150 °C	249.79	5.91	254.19	5.65
	High HI—250 °C	248.66	4.76	246.95	5.03
	Low HI—100 °C	257.00	4.00	258.78	5.49
	Low HI—150 °C	253.75	5.21	255.34	5.23
	Low HI—250 °C	254.22	4.41	255.13	4.22

WFS leads to a higher HI. Similar to Fe%, the material chemistry is the major contributor to the resulting hardness.

Table 8 lists the average values of HV_3. Material G2205 has higher values than G2209. However, it seems that the IT does not significantly affect HV_3 regardless of the selected material. The vertical lines do not exhibit significant variation of the HV_3 test along the wall of each specimen, excluding the diluted layer, revealing a homogeneous behavior.

3.6 Microstructure characterization

Before microstructural characterization, etching with Beraha's II appeared to be a challenge for the large areas of the wall cross-section. A first strategy consisting of reproducing the optimized etching cycle and proposed by Varbai et al. [55] led to a strong variation in contrast between the two materials G2205 and G2209. This behavior is interpreted as caused by the differences of ferrite content between the materials, of around 20%. As the chemical agent is preferably interacting with the ferrite phase while keeping the austenite phase unetched, the variation of

reactive surface affects the optimal etching time. Using the etching procedure proposed in Section 2.3.2 produced some improvement, but depending on the sample etched, a variation in contrast was still observed and led to falsely counted phases.

Images with higher contrast were selected for the method comparison between image analysis and Feritscope© measurements. The results are shown in Fig. 13a. Three locations similar to the microstructural analysis were chosen in the bottom, middle, and top area of each sample cross-section. The objective of the comparison was to assess the reliability of the Feritscope© measurements. Samples were selected including different IT and high HI (i.e., 0.23 kJ/mm – nominal value) as well as low HI (i.e., 0.09 kJ/mm – nominal value). The Feritscope© results show a difference of between -5% and +20% compared to the estimated Fe% using the image analysis method. These measurements were conducted at the same location as the corresponding image analysis and consist of single measures. Earlier research [56, 57] has reported a suggested correction factor of 10%, but our study shows a stronger variation in the results. This discrepancy is rooted in the irregularly etched surface leading to misinterpretation of the phases. Human error can affect the microstructural characterization due to (i) slight deviations in the etching process and (ii) variation of the microstructural examination and especially the image attributes (brightness, focus, intensity). Automated measurements can help reduce this error. Thresholding of the image analysis and Fe% was carried out as shown in Fig. 13b and as described in the material and method section.

During the microstructural investigation, color etching led to brown coloration of the δ-ferrite while leaving the austenite brightly colored, as seen in Figs. 14 and 15. No significant welding defects in the cross-section could be reported. As previously mentioned, Fe% is higher in the G2205 material samples in every area of the cross-sections. The austenite morphology varies within the micrographs due to (i) grain boundary austenite nucleated from the initial δ-ferrite columnar grains, followed by (ii) Widmanstätten austenite needles.
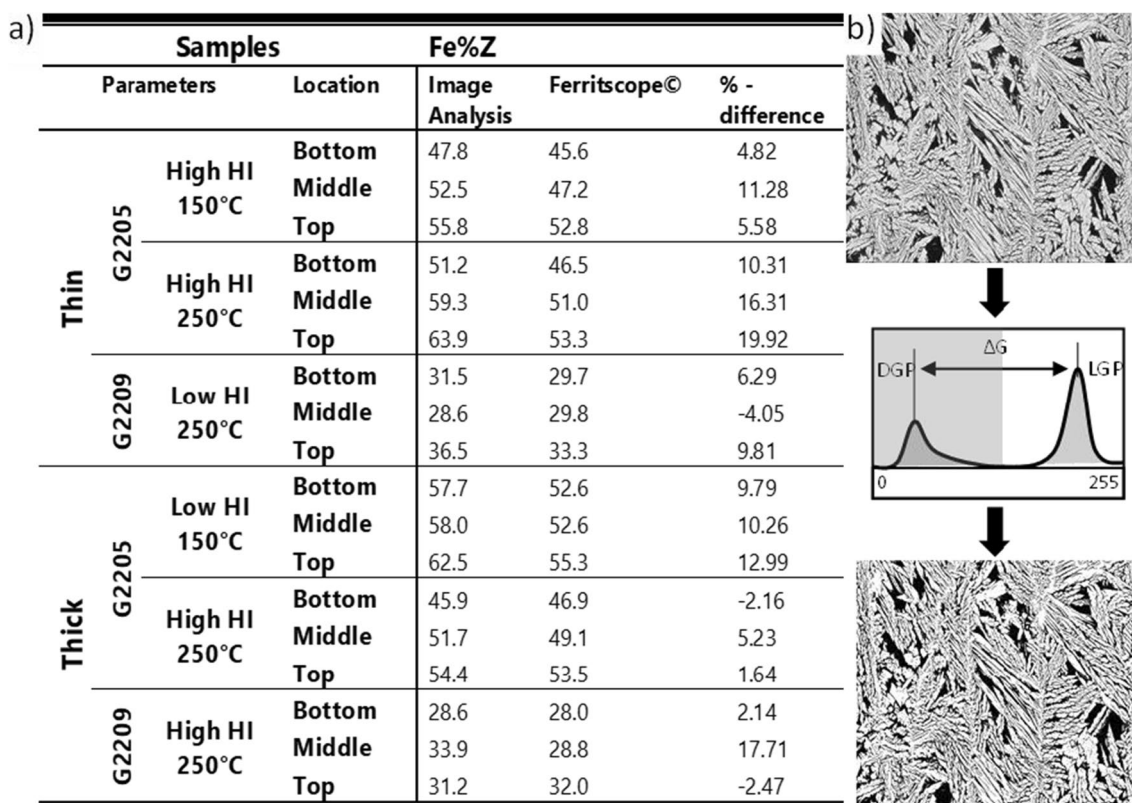
Samples			Fe%Z		
Parameters		Location	Image Analysis	Ferritscope©	% - difference
Thin	G2205	High HI 150°C	Bottom	47.8	45.6	4.82
			Middle	52.5	47.2	11.28
			Top	55.8	52.8	5.58
		High HI 250°C	Bottom	51.2	46.5	10.31
			Middle	59.3	51.0	16.31
			Top	63.9	53.3	19.92
	G2209	Low HI 250°C	Bottom	31.5	29.7	6.29
			Middle	28.6	29.8	-4.05
			Top	36.5	33.3	9.81
Thick	G2205	Low HI 150°C	Bottom	57.7	52.6	9.79
			Middle	58.0	52.6	10.26
			Top	62.5	55.3	12.99
		High HI 250°C	Bottom	45.9	46.9	-2.16
			Middle	51.7	49.1	5.23
			Top	54.4	53.5	1.64
	G2209	High HI 250°C	Bottom	28.6	28.0	2.14
			Middle	33.9	28.8	17.71
			Top	31.2	32.0	-2.47

Fig. 13 Comparison of ferrite content between image analysis method and Feritscope© results: **a** table; **b** thresholding—image analysis method

Fig. 14 Micrographs of each tested material in three main areas: bottom, middle, and top section—×200 magnification, high HI, 250 °C IT
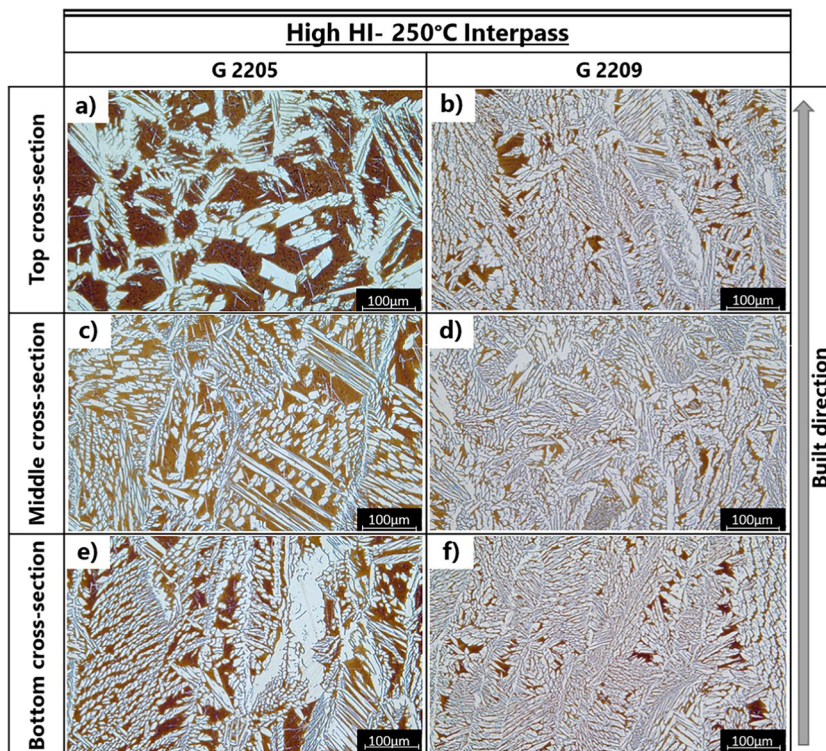
Finally, thinner intragranular austenite can be observed as well as secondary austenite (γ_2) in Figs. 14a and 15c. However, more γ_2 is seen in the low HI samples. This secondary phase is known for promoting pitting corrosion but was not evaluated in this study. The optical microscopic observations did not reveal visible precipitations.

Coarser primary ferrite dendrites are seen in Fig. 14 in the high HI samples in both materials and are more noticeable with G2205 compared with Fig. 15 at lower HI. The manufacturing parameters influence the cooling rate and the temperature gradient during solidification. Hence, a lower HI (see Fig. 15) results in a faster cooling rate during solidification, refining the dendrite size compared with the highest HI (see Fig. 14) while keeping a similar dendritic morphology.

Coarser microstructure means larger grains and consequently less grain boundaries which affects the movement of dislocations through the material. Therefore, the resistance to deformation of the low heat input samples is higher than for the high heat input samples, resulting in higher hardness, as revealed in Fig. 12. The relationship between the grain size and hardness is complex and depends also on the selected material. The ferrite-to-austenite ratio tends also to influence the resulting hardness. However, the composite response of the material to macrohardness testing can be influenced by various grain boundaries and phases located within the volume beneath the hardness indent.

3.7 Nitrogen and oxygen variation

Nitrogen and oxygen content in the matrix is finally proposed for two configurations, high and low HI, for both materials for thick samples and compared with the wire. Figure 16 shows the resulting variation in nitrogen and oxygen content. Additional testing of the wire was performed as reference and for validation of the initial data sheet (Table 1). Figure 16a shows how the nitrogen content of the deposited walls has increased in every tested configuration by 10 to 18% compared with the wire. While the high HI sample of G2205 shows a stronger increase in nitrogen than the low HI configuration, both high and low HI samples of G2209 reveal similar gains in nitrogen. The corresponding ferrite percentage is 48.5% and 52.66% for high and low HI, respectively, on G2205, but 28.9% and 30.55% respectively on G2209. The present study cannot highlight any positive or negative impact of nitrogen variation in the final ferrite percentage for a thick sample and the selected parameters. The impact of nitrogen in the shielding gas has yet to be confirmed, as similar results have been reported [20] with a nitrogen-free shielding gas. Further investigations should focus on the influence of nitrogen in DSS manufactured with WAAM to assess the influence of adding nitrogen to the shielding gas.

Figure 16b shows how the oxygen content increased sharply on the deposited walls compared with the wire measurements. The trend shows an average increase across

Fig. 15 Micrographs of each tested material in three main areas: bottom, middle, and top section—×200 magnification, low HI, 100 °C IT
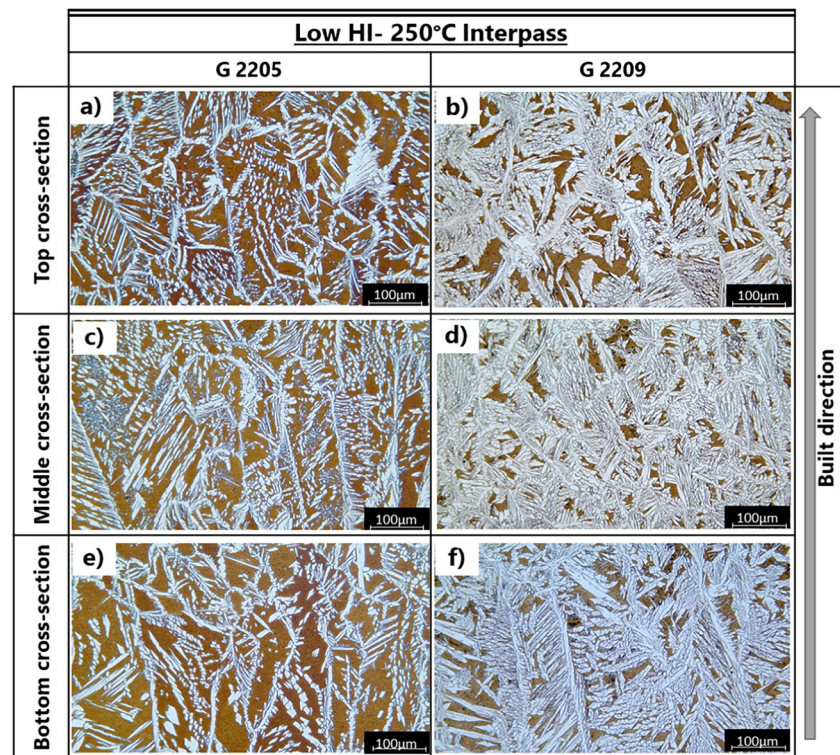
Fig. 16 Nitrogen (**a**) and oxygen (**b**) composition of welded samples in weight percent compared with the measured wire chemical composition
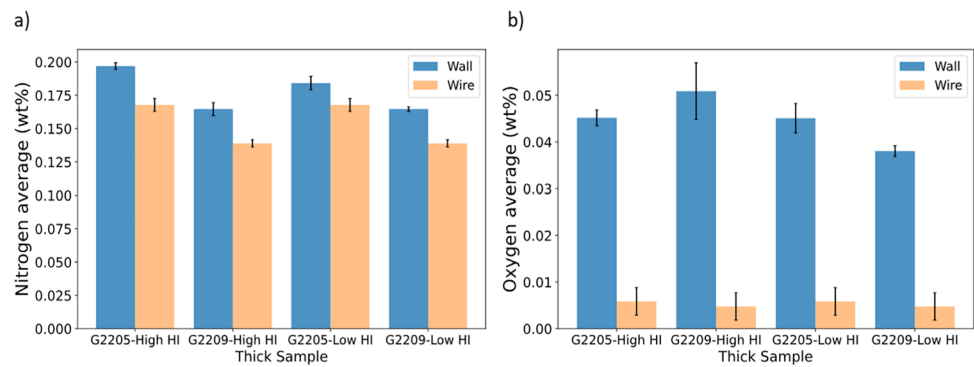
measured samples of 0.04 wt% of oxygen in the deposited walls compared with the measured oxygen content in the wire. Similarly, previous research [20] has reported a similar oxygen content. During manufacturing, no cleaning was done between layers, leading to an oxidized layer on the surface of each run. This practice can promote an increase of oxygen in the deposited material. The pitting corrosion resistance is known to be reduced with higher oxygen content [30].

4 Conclusions

This article examined the effect of process parameters, including different DSS chemistries, wire feed rates, travel speeds, and interpass temperatures, on the processing of thick and thin walls built by WAAM. The objective was to evaluate the resulting macroscale geometrical results (i.e., resulting layer thickness, over-thickness and deposition rates) as a function of the process parameters. Additionally, microscale mechanical properties are reported involving hardness (HV_3), resulting average Ferrite content (Fe%) and distribution, variation of nitrogen and oxygen in the matrix, and optical microstructural characterization. The main global contributions of this research are as follows:

- The tested window of operation (i.e., 0.09 kJ/mm ≥ HI ≥ 0.23 kJ/mm—nominal value) provides reliable results for both wire chemistries of G2205 and G2209.
- The statistical analysis shows that heat input (HI) as a thermodynamic parameter can be used to explain the variability of the selected response variables, especially macro-dimensional results, such as layer thickness and over-thickness.
- Travel speed (TS) and wire feed speed (WFS) show high statistical significance, thus driving the variation of macro- and microperformance variables. TS and WFS show often opposing effects on the performance variables. Increasing WFS has a direct effect on achievable layer height and over-thickness, whereas increasing TS

has the reverse effect. Interpass temperature (IT) and CAD thickness show a decreased statistical significance in comparison.

- The maximum achieved average instantaneous deposition rate combining both wire chemistries is 3.54 kg/h using the highest WFS = 7.4 m/min and the slowest TS = 720 mm/min. The average value of the global deposition is 0.36 kg/h. While the instantaneous deposition rates are not affected by the part geometry (i.e., thinner or thicker walls), higher global deposition rates can be achieved when processing thick walls versus thin walls (i.e., 0.5kg/h and 0.2kg/h respectively).
- The longitudinal and transverse Fe% maps show that both the part geometry and the manufacturing weaving strategy affect the homogeneous spatial distribution of Fe%. The weaving pattern is visible in the longitudinal plane and the observed trend is that Fe% spatial distribution is more heterogeneous in samples produced with low HI.

Further contributions regarding the impact of process parameters including path planning, build strategies, and wire chemical composition on the studied microstructural and mechanical aspects are as follows:

- G2205 (i.e., wire chemistry with increased nickel content) shows a stable austenite-to-ferrite ratio of equal proportions (i.e., average Fe% = 49.20 ± 1.92%), whereas G2209 provides a reduced ferrite content (i.e., average Fe% = 29.69 ± 0.56%).
- Fe% appears to be sensible to a variation of WFS and TS for both materials G2205 and G2209. The variation of Fe% is linearly correlated to the applied energy. Increasing energy leads to a decrease of Fe% and HV_3. Furthermore, Fe% and HV_3 are positively correlated. Hence, increasing the Fe% by changing the process parameters leads to higher HV_3 of the manufacturing samples. G2205 has an average HV_3 = 252.8 ± 3.55, whereas G2209 has an HV_3 = 241.6 ± 3.17.

- The microstructural analysis confirms a higher ferrite content in G2205 compared with G2209. High HI samples reveal coarser structures caused by slower cooling rates and longer time at high temperatures. Both materials show a dendritic morphology.
- The average nitrogen and oxygen content increased in the deposited thick walls for both selected materials with high and low HI.

The implemented OFAT DoE was suitable for screening and exploration. Future research is planned to implement a more robust central composite DoE to explore the interactions between process parameters. Future experiments are required to develop quantitative predictive models for macro- and microperformance variables using surface response methods or machine learning methods. Macro-dimensional deviation (i.e., achievable layer height and over-thickness) could be modeled effectively using HI (i.e., $R^2 \geq 0.85\%$). Future experiments will allow us to capture this variable considering the interrelations between process variables and, therefore, to create a predictive model to dynamically control the stick-out or tip-to-work distance during the process.

Additionally, full industrialization of DSS with WAAM would require the study of additional process and mechanical performance variables including additional (i) path planning strategies, (ii) impact of process variables on surface quality and morphology, (iii) integration of machining aspects, (iv) tensile properties, (v) long-term corrosion testing, and (vi) in-depth microstructural analysis. Furthermore, the presence of intermetallic precipitates (such as sigma phase (σ), chi (κ), π) was not investigated in this study, which could lead to detrimental pitting corrosion effects in DSS. Overall, this research shows that tailoring of the wire chemistry by lowering the nickel content in material G2205 provided an equal austenite-to-ferrite ratio of equal proportions with increased HV compared to G2209. The weaving strategy influences the local material structure, showing a heterogeneous distribution of ferrite. The complex thermal history in metal additive manufacturing, limited information on process and response variables, wide uncertainties, and higher-dimensional design spaces need to be fully understood to drive metal WAAM toward full industrialization, to reliably manufacture large complex metal structures with complex build strategies.

Supplementary Information The online version contains supplementary material available at https://doi.org/10.1007/s00170-023-11560-5.

Data availability The raw/processed data required to reproduce these findings cannot be shared at this time as the data also forms part of an ongoing study. Data can be made available upon request.

Declarations

Competing interests The authors declare no competing interests.

References

1. Flores I, Kretzschmar N, Azman AH et al (2020) Implications of lattice structures on economics and productivity of metal powder bed fusion. Addit Manuf 31:100947. https://doi.org/10.1016/j.addma.2019.100947

2. Queguineur A, Rückert G, Cortial F, Hascoët JY (2018) Evaluation of wire arc additive manufacturing for large-sized components in naval applications. Weld World 62:259–266. https://doi.org/10.1007/s40194-017-0536-8

3. Cederberg E, Hosseini VA, Kumara C, Karlsson L (2020) Physical simulation of additively manufactured super duplex stainless steels – microstructure and properties. Addit Manuf 34:101269. https://doi.org/10.1016/j.addma.2020.101269

4. Ahn DG (2021) Directed energy deposition (DED) process: state of the art. Int J Precis Eng Manuf - Green Technol 8:703–742. https://doi.org/10.1007/s40684-020-00302-7

5. Rodrigues TA, Duarte VR, Miranda RM et al (2021) Ultracold-wire and arc additive manufacturing (UC-WAAM). J Mater Process Technol 296:117196. https://doi.org/10.1016/j.jmatprotec.2021.117196

6. Rodrigues TA, Cipriano Farias FW, Zhang K et al (2022) Wire and arc additive manufacturing of 316L stainless steel/Inconel 625 functionally graded material: development and characterization.

J Mater Res Technol 21:237–251. https://doi.org/10.1016/j.jmrt.2022.08.169

7. Zuo X, Zhang W, Chen Y et al (2022) Wire-based directed energy deposition of NiTiTa shape memory alloys: microstructure, phase transformation, electrochemistry, X-ray visibility and mechanical properties. Addit Manuf 59:103115. https://doi.org/10.1016/j.addma.2022.103115

8. Li S, Li JY, Jiang ZW et al (2022) Controlling the columnar-to-equiaxed transition during directed energy deposition of Inconel 625. Addit Manuf 57:102958. https://doi.org/10.1016/j.addma.2022.102958

9. Evans SI, Wang J, Qin J et al (2022) A review of WAAM for steel construction – manufacturing, material and geometric properties, design, and future directions. Structures 44:1506–1522. https://doi.org/10.1016/j.istruc.2022.08.084

10. Queguineur A, Marolleau J, Lavergne A, Rückert G (2020) Evaluation of tandem controlled short-circuit GMAW for improved deposition in additive manufacture of large Nickel Aluminium Bronze naval components. Weld World 64:1389–1395. https://doi.org/10.1007/s40194-020-00925-z

11. Ding D, Pan Z, van Duin S et al (2016) Fabricating superior NiAl bronze components through wire arc additive manufacturing. Materials 9. https://doi.org/10.3390/ma9080652

12. Martina F, Ding J, Williams S et al (2019) Tandem metal inert gas process for high productivity wire arc additive manufacturing in stainless steel. Addit Manuf 25:545–550. https://doi.org/10.1016/j.addma.2018.11.022

13. Ding D, Pan Z, Cuiuri D, Li H (2015) Wire-feed additive manufacturing of metal components: technologies, developments and future interests. Int J Adv Manuf Technol 81:465–481. https://doi.org/10.1007/s00170-015-7077-3

14. Pattanayak S, Sahoo SK (2021) Gas metal arc welding based additive manufacturing—a review. CIRP J Manuf Sci Technol 33:398–442. https://doi.org/10.1016/j.cirpj.2021.04.010

15. Imoudu NE, Ayele YZ, Barabadi A (2018) The characteristic of cold metal transfer (CMT) and its application for cladding. IEEE Int Conf Ind Eng Eng Manag:1883–1887. https://doi.org/10.1109/IEEM.2017.8290218

16. Odermatt AE, Ventzke V, Dorn F et al (2021) Effect of laser beam welding on microstructure, tensile strength and fatigue behaviour of duplex stainless steel 2205. J Manuf Process 72:148–158. https://doi.org/10.1016/j.jmapro.2021.10.020

17. Da Fonseca GS, Barbosa LOR, Ferreira EA et al (2017) Microstructural, mechanical, and electrochemical analysis of duplex and superduplex stainless steels welded with the autogenous TIG process using different Heat Input. Metals 7(12):538. https://doi.org/10.3390/met7120538

18. Wang S, Ma Q, Li Y (2011) Characterization of microstructure, mechanical properties and corrosion resistance of dissimilar welded joint between 2205 duplex stainless steel and 16MnR. Mater Des 32:831–837. https://doi.org/10.1016/j.matdes.2010.07.012

19. Shen J, Gonçalves R, Choi YT et al (2022) Microstructure and mechanical properties of gas metal arc welded CoCrFeMnNi joints using a 410 stainless steel filler metal. Mater Sci Eng A 857:144025. https://doi.org/10.1016/j.msea.2022.144025

20. Posch G, Chladil K, Chladil H (2017) Material properties of CMT—metal additive manufactured duplex stainless steel blade-like geometries. Weld World 61:873–882. https://doi.org/10.1007/s40194-017-0474-5

21. Pechet G, Hascoet J-Y, Rauch M et al (2020) Manufacturing of a hollow propeller blade with WAAM process - from the material characterisation to the achievement. Ind 40 – Shap Future Digit World:155–160. https://doi.org/10.1201/9780367823085-28

22. Stuzer J, Totzauer T, Wittig B et al (2019) GMAW cold wire technology for adjusting the manufactured duplex stainless steel components. Metals 9:564–583

23. Zhang D, Liu A, Yin B, Wen P (2022) Additive manufacturing of duplex stainless steels - a critical review. J Manuf Process 73:496–517. https://doi.org/10.1016/j.jmapro.2021.11.036

24. Kang DH, Lee HW (2012) Effect of different chromium additions on the microstructure and mechanical properties of multipass weld joint of duplex stainless steel. Metall Mater Trans Phys Metall Mater Sci 43:4678–4687. https://doi.org/10.1007/s11661-012-1310-6

25. Pérez-Ruiz JD, de Lacalle LNL, Urbikain G et al (2021) On the relationship between cutting forces and anisotropy features in the milling of LPBF Inconel 718 for near net shape parts. Int J Mach Tools Manuf 170:103801. https://doi.org/10.1016/j.ijmachtools.2021.103801

26. Traidia A, Roger F, Chidley A (2011) Effect of helium-argon mixtures on the heat transfer and fluid flow in Gas Tungsten Arc Welding. World Acad Sci Eng Technol 73:1053–1059

27. Valiente Bermejo MA, Karlsson L, Svensson LE et al (2015) Effect of shielding gas on welding performance and properties of duplex and superduplex stainless steel welds. Weld World 59:239–249. https://doi.org/10.1007/s40194-014-0199-7

28. Bhatt RB, Kamat HS, Ghosal SK, De PK (1999) Influence of nitrogen in the shielding gas on corrosion resistance of duplex stainless steel welds. J Mater Eng Perform 8:591–597. https://doi.org/10.1007/s11665-999-0014-6

29. Hosseini A, Högström M, Hurtig K et al (2019) Wire-arc additive manufacturing of a duplex stainless steel: thermal cycle analysis and microstructure characterization. Weld World 63:975–987. https://doi.org/10.1007/s40194-019-00735-y

30. Jeon SH, Hur DH, Kim HJ, Park YS (2014) Influence of oxygen content on the inclusion formation and pitting corrosion resistance of hyper duplex stainless steels. Mater Trans 55:1872–1877. https://doi.org/10.2320/matertrans.M2014164

31. Xia Y, Amatsu K, Miyasaka F, Mori H (2021) Effect of nitrogen on weldability and the microstructure in laser beam welding of duplex stainless steel. Miner Met Mater Ser:201–209

32. Norrish J, Cuiuri D (2014) The controlled short circuit GMAW process: a tutorial. J Manuf Process 16:86–92. https://doi.org/10.1016/j.jmapro.2013.08.006

33. Norrish J, Polden J, Richardson I (2021) A review of wire arc additive manufacturing: development, principles, process physics, implementation and current status. J Phys Appl Phys 54:473001. https://doi.org/10.1088/1361-6463/ac1e4a

34. Eriksson M, Lervåg M, Sørensen C et al (2018) Additive manufacture of superduplex stainless steel using WAAM. MATEC Web Conf 188:1–8. https://doi.org/10.1051/matecconf/201818803014

35. Jafari D, Vaneker THJ, Gibson I (2021) Wire and arc additive manufacturing: opportunities and challenges to control the quality and accuracy of manufactured parts. Mater Des 202:109471. https://doi.org/10.1016/j.matdes.2021.109471

36. Zhang Y, Cheng F, Wu S (2021) Improvement of pitting corrosion resistance of wire arc additive manufactured duplex stainless steel through post-manufacturing heat-treatment. Mater Charact 171:110743. https://doi.org/10.1016/j.matchar.2020.110743

37. Hejripour F, Binesh F, Hebel M, Aidun DK (2019) Thermal modeling and characterization of wire arc additive manufactured duplex stainless steel. J Mater Process Technol 272:58–71. https://doi.org/10.1016/j.jmatprotec.2019.05.003

38. Nikam PP, Arun D, Ramkumar KD, Sivashanmugam N (2020) Microstructure characterization and tensile properties of CMT-based wire plus arc additive manufactured ER2594. Mater Charact 169:110671. https://doi.org/10.1016/j.matchar.2020.110671

39. Zhang Y, Cheng F, Wu S (2021) The microstructure and mechanical properties of duplex stainless steel components fabricated via flux-cored wire arc-additive manufacturing. J Manuf Process 69:204–214. https://doi.org/10.1016/j.jmapro.2021.07.045

40. Kumar P, Maji K (2023) Experimental investigations and parametric effects on depositions of super duplex stainless steel in

wire arc additive manufacturing. Proc Inst Mech Eng Part E J Process Mech Eng 095440892311582. https://doi.org/10.1177/09544089231158253

41. Vinoth Jebaraj A, Ajaykumar L, Deepak CR, KVV A Weldability, machinability and surfacing of commercial duplex stainless steel AISI2205 for marine applications – a recent review. J Adv Res 8:183–199. https://doi.org/10.1016/j.jare.2017.01.002

42. Srinivasan D, Sevvel P, Solomon IJ, Tanushkumaar P (2022) Materials today : proceedings a review on cold metal transfer (CMT) technology of welding. Mater Today Proc. https://doi.org/10.1016/j.matpr.2022.04.016

43. Pickin CG, Williams SW, Lunt M (2011) Characterisation of the cold metal transfer (CMT) process and its application for low dilution cladding. J Mater Process Technol 211:496–502. https://doi.org/10.1016/j.jmatprotec.2010.11.005

44. Verma J, Taiwade RV (2017) Effect of welding processes and conditions on the microstructure, mechanical properties and corrosion resistance of duplex stainless steel weldments—a review. J Manuf Process 25:134–152. https://doi.org/10.1016/j.jmapro.2016.11.003

45. Yang Y, Yan B, Li J, Wang J (2011) The effect of large heat input on the microstructure and corrosion behaviour of simulated heat affected zone in 2205 duplex stainless steel. Corros Sci 53:3756–3763. https://doi.org/10.1016/j.corsci.2011.07.022

46. Mohanty G, Besra L, Bhattacharjee S, Singh BP (2008) Optimization of electrophoretic deposition of alumina onto steel substrates from its suspension in iso-propanol using statistical design of experiments. Mater Res Bull 43:1814–1828. https://doi.org/10.1016/j.materresbull.2007.07.014

47. Ostolaza M, Arrizubieta JI, Quegueineur A et al (2022) Influence of process parameters on the particle–matrix interaction of WC-Co metal matrix composites produced by laser-directed energy deposition. Mater Des 223:111172. https://doi.org/10.1016/j.matdes.2022.111172

48. Antony J (2014) Screening designs. Design of experiments for engineers and scientists. Elsevier, In, pp 51–62

49. Haghdadi N, Laleh M, Chen H et al (2021) On the pitting corrosion of 2205 duplex stainless steel produced by laser powder bed fusion additive manufacturing in the as-built and post-processed conditions. Mater Des 212:110260. https://doi.org/10.1016/j.matdes.2021.110260

50. Argandoña G, Palacio JF, Berlanga C et al (2017) Effect of the temperature in the mechanical properties of austenite, ferrite and sigma phases of duplex stainless steels using hardness, microhardness and nanoindentation techniques. Metals 7. https://doi.org/10.3390/met7060219

51. Pohl M, Storz O, Glogowski T (2007) Effect of intermetallic precipitations on the properties of duplex stainless steel. Mater Charact 58:65–71. https://doi.org/10.1016/j.matchar.2006.03.015

52. Zanotto F, Grassi V, Merlin M et al (2015) Effect of brief heat treatments performed between 650 and 850°C on corrosion behaviour of a lean duplex stainless steel. Corros Sci 94:38–47. https://doi.org/10.1016/j.corsci.2015.01.035

53. Knyazeva M, Pohl M (2013) Duplex steels. Part II: Carbides and nitrides. Metallogr Microstruct Anal 2:343–351. https://doi.org/10.1007/s13632-013-0088-2

54. Di Cocco V, Iacoviello F, Ischia G (2017) Duplex stainless steels "475°C embrittlement": influence of the chemical composition on the fatigue crack propagation. Procedia Struct Integr 3:299–307. https://doi.org/10.1016/j.prostr.2017.04.051

55. Varbai B, Pickle T, Májlinger K (2018) Development and comparison of quantitative phase analysis for duplex stainless steel weld. Period Polytech Mech Eng 62:247–253. https://doi.org/10.3311/PPme.12234

56. Kaňa V, Pernica V, Zadera A, Krutiš V (2019) Comparison of methods for determining the ferrite content in duplex cast steels. Arch Foundry Eng 19:85–90. https://doi.org/10.24425/afe.2019.127121

57. Putz A, Althuber M, Zelić A et al (2019) Methods for the measurement of ferrite content in multipass duplex stainless steel welds. Weld World 63:1075–1086. https://doi.org/10.1007/s40194-019-00721-4

58. Del Sol I, Rivero A, López De Lacalle LN, Gamez AJ (2019) Thin-wall machining of light alloys: a review of models and industrial approaches. Materials 12:2012. https://doi.org/10.3390/ma12122012

59. Asadi R, Niknam SA, Anahid MJ, Ituarte IF (2023) The use of wavelet transform to evaluate the sensitivity of acoustic emission signals attributes to variation of cutting parameters in milling aluminum alloys. Int J Adv Manuf Technol. https://doi.org/10.1007/s00170-023-11305-4